PHYSICAL REVIEW A **107**, 023513 (2023)

Tracking nanoscale perturbation in active disordered media

Renu Yadav,[1] Patrick Sebbah,[2] Maruthi M. Brundavanam,[1] and Shivakiran Bhaktha B. N.[1,*]
[1]*Department of Physics, Indian Institute of Technology Kharagpur, Kharagpur-721302, India*
[2]*Department of Physics, The Jack and Pearl Resnick Institute for Advanced Technology,*
Bar-Ilan University, Ramat-Gan, 5290002 Israel

(Received 1 October 2022; accepted 27 January 2023; published 16 February 2023)

Disorder-induced feedback makes random lasers very susceptible to any changes in the scattering medium. The sensitivity of the lasing modes to perturbations in the disordered systems has been utilized to map the regions of perturbation. A tracking parameter that takes into account the cumulative effect of changes in the spatial distribution of the lasing modes of the system has been defined to locate the region in which a scatterer is displaced by a few nanometers. We show numerically that the precision of the method increases with the number of modes. The proposed method opens up the possibility of application of random lasers as a tool for monitoring locations of nanoscale displacement, which can be useful for single-particle detection and monitoring.

DOI: 10.1103/PhysRevA.107.023513

I. INTRODUCTION

A random laser (RL) is an optical device that utilizes the disorder in the system for the optical feedback. Unlike conventional lasers, no well-defined cavities are present in RLs. The idea of feedback by multiple scattering was first proposed by Letokhov [1] and has been extensively used to realize random lasing in a variety of disordered systems [2–8]. Two types of RLs have been reported, namely, coherent RLs and incoherent RLs, depending on whether the scattering induces feedback in the field or the intensity, respectively [9]. The scattering strength determines the lasing characteristics such as lasing threshold of the system, spatial confinement of the modes, etc. Based on the scattering strength, disordered systems can be broadly divided into two categories, namely, strongly scattering and weakly scattering systems. In the strongly scattering systems the lasing modes are localized well within the system and are identical to the quasi-bound (QB) states of the passive system [10–12], whereas in weakly scattering systems the lasing modes extend all over the system [12,13].

Unlike conventional lasers, RL emission is random in wavelength, omnidirectional [4], and has low spatial and temporal coherence [14–16]. These properties make them suitable for different applications such as imaging [17], displays and lighting [18], holography [19], etc., but it limits their use where specific wavelength or unidirectional emission is required. Spatial light modulators (SLMs) have been used to shape the pump intensity profile to control the emission and directionality of RLs, making them useful for different applications [20–26]. As the feedback in RLs is provided by disorder-induced scattering, the lasing modes are very sensitive to any changes in the scattering medium. This makes RLs a natural candidate for designing sensors for various applications. The strong dependence of emission characteristics of RLs on the scattering properties of the medium have been utilized to assess nanoscale perturbations [27]. The monitoring of single-nanoparticle perturbation enables to detect a single virus, bacterium, and biomolecule. Random lasers have been used as a diagnostic tool for bioimaging and biosensing in various biological structures infiltrated with dye [5,28,29]. The nanoscale deformation and prefailure damage in bones can be detected by monitoring the shifts in the random lasing peaks [30]. In *ex vivo* dye-infiltrated human tissues, changes in the emission spectrum have been observed in malignant tissues as compared to the healthy ones [31]. The cancerous tissues of different grades of malignancy can be differentiated as they exhibit different lasing spectra for the same pump energy [32]. RLs have been proposed as an *in vivo* tool to differentiate between skin, fat, muscle, and nerve tissues during laser surgery [33].

In this work, RLs have been proposed as a tool to map the regions of nanoscale perturbation in several random media. A two-dimensional (2D) active disordered system has been considered and nanoscale perturbations have been introduced in the medium. Using the finite difference time domain (FDTD) method [34], the modes and the corresponding spatial field distributions for the system before and after the perturbation have been computed. In the past, RLs have been used to detect changes in the scattering medium [27]. In this work we go a step further and show numerically that it is also possible to identify the position of the perturbation with good precision. A small perturbation in the system leads to minute changes in the spectral position of the modes and their corresponding spatial field distributions, but the individual modes do not provide any information about the location of the perturbation. So, a tracking parameter is defined which takes into account the cumulative effect of changes in the modes, to map the region of perturbation. We find that its mapping converges to the defect location when the number of modes increases. This finding paves the way to single-particle tracking in disordered systems. The theoretical explorations in this work provide an

---

[*] kiranbhaktha@phy.iitkgp.ac.in

©2023 American Physical Society

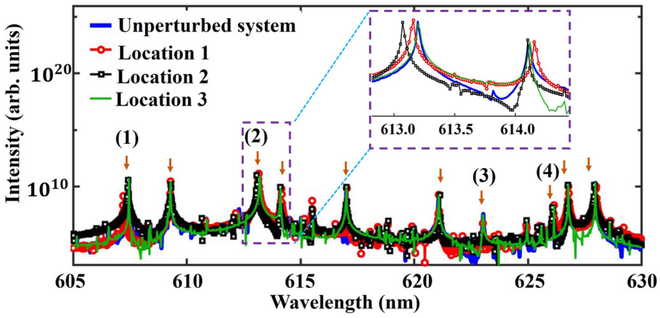

FIG. 1. Emission spectra of the unperturbed system and the system with a single particle perturbed by 10 nm at three different locations in the system. Ten peaks considered are marked with arrows. The labeled modes are (1) 607.45 nm, (2) 613.20 nm, (3) 623.01 nm, and (4) 626.13 nm. The inset shows the magnified image of the region marked with a dashed magenta line. It shows the spectral shift of the mode as the perturbation is introduced in the system.

initial framework to utilize RLs in the field of diagnostics to monitor and track the growth of tumors in disordered biological systems.

II. NUMERICAL METHOD AND COMPUTATIONAL DETAILS

A 2D disordered system of size $L^2 = 5 \times 5$ μm^2 has been considered. It consists of circular particles with radius $r = 60$ nm and refractive index $n_2 = 2.54$, randomly distributed in a background medium of refractive index $n_1 = 1.53$ as shown in Fig. 7 in the Appendix. The values of the refractive index have been chosen to mimic the presence of TiO_2 particles in 4-(dicyanomethylene)-2-methyl-6-(4-dimethylaminostyryl)-4H-pyran (DCM)-doped polyvinyl alcohol (PVA) thin films [35–37]. The background medium has been chosen as the active part of the system and modeled as a four-level atomic system. An active medium has been considered here, because it is quite difficult to excite passive modes of the system experimentally. The passive modes have leakage and are short lived due to out-of-plane scattering. Even on neglecting this out-of-plane scattering numerically, a few modes, especially at the edge of the sample, may not be identified. The active medium paves the way to study all the possible modes of the system through lasing. The surface-filling fraction of the scatterers is 28%. In this study, 2D FDTD computation has been carried out using transverse magnetic fields with a grid resolution of $\Delta x = \Delta y = 10$ nm, along the x and y directions, respectively. In order to ensure the stability of the simulation, the time step chosen is $\Delta t = 2.37 \times 10^{-17}$ s [38]. The parameters used for the active medium are mentioned in Ref. [10]. The system is pumped uniformly with a Gaussian pulse of central wavelength 532 nm and pulse duration $\sim 10^{-15}$ s at a pump level above the lasing threshold of the system. Further details on the computational algorithm and numerical parameters are provided in the Appendix.

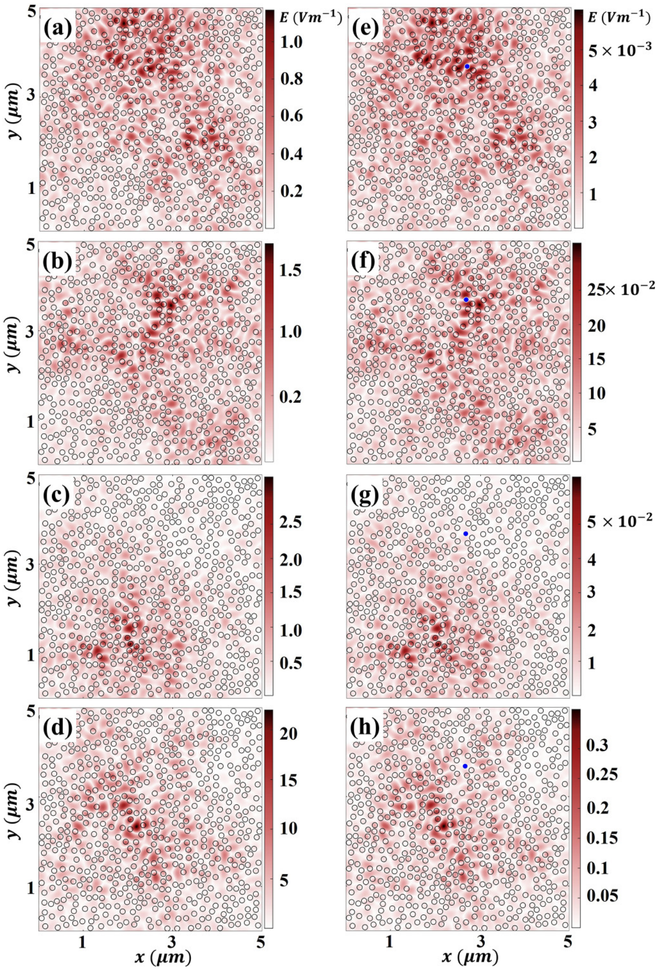

FIG. 2. Spatial field distribution of modes marked as 1–4 in Fig. 1, (a–d) before and (e–h) after a single particle is displaced by 10 nm. The perturbed particle is marked in blue.

III. RESULTS AND DISCUSSION

The 2D active random system was pumped above the lasing threshold. The energy in the system was observed to grow exponentially, and after some strong relaxation oscillations, it eventually reached a steady state as shown in Fig. 8 in the Appendix. The lasing modes of the system are calculated by the Fourier transform of the time records of the field after the system has reached the stationary state. Several distinct peaks are observed as shown in Fig. 1. The ten modes considered for further analysis are marked with arrows. The discrete peaks in the emission spectrum indicate lasing action with resonant feedback. The spatial field distribution of the modes is computed by taking the Fourier transform of the field recorded at each grid point. The spatial field distribution of the modes marked as 1–4 in Fig. 1 is shown in Figs. 2(a)–2(d). It is observed that the modes are confined well within the system, indicating that the system is strongly scattering. The numerically computed scattering mean free path for the system using the Mie scattering theory is $l_s \approx 0.3$ μm [39]. The localization length for the system is calculated by considering the field intensity profiles of modes averaged along the x or y directions. The averaged intensity profile exhibits strong local fluctuations, but its envelope decays exponentially, whose characteristic length gives the localization length of the modes. The average localization length calculated for the system is $\xi \approx 2.6$ μm. The scattering mean free path and the localization length also indicate that the system is strongly scattering and the modes are confined well within the system, respectively.

Next, in order to introduce a single-nanoscale perturbation in the system, a randomly chosen scatterer was displaced by 10 nm along an arbitrary direction. The numerical parameters limit the minimum and the maximum perturbation that can be introduced in the system. The minimum displacement cannot be smaller than the grid resolution, and the maximum displacement possible is dependent on the surface filling fraction of the system. In realistic systems, such limitations do not exist and hence it is expected that even smaller perturbations can be detected. The effect of perturbation at different locations in the system on the RL spectra and spatial field distribution of modes has been studied. The emission spectra of the system when a single particle is perturbed at three different locations in the system are shown in Fig. 1. It is observed that the perturbation causes a slight shift in the spectral positions of the random lasing modes, as shown in the inset. Modes 1–4 experience spectral shifts ($\Delta\lambda$) of magnitude 0.239, 0.039, 0.004, and 0.004 nm, respectively. Further details on the correspondence between the magnitude of the spectral shifts and the mode field distributions are presented later.

The perturbation also leads to changes in the spatial field distribution of modes as shown in Figs. 2(e)–2(h), for the perturbation at location 1 (Fig. 1), wherein the perturbed particle is marked in blue. In order to quantify the changes in the system due to perturbation, the 2D correlation coefficient (C_E) between the spatial field distribution of modes before and after perturbation is calculated, which is defined as

$$C_E = \frac{\sum_x \sum_y [E(x,y) - \bar{E}][E'(x,y) - \bar{E}']}{\sqrt{\{\sum_x \sum_y [E(x,y) - \bar{E}]^2\}\,\{\sum_x \sum_y [E'(x,y) - \bar{E}']^2\}}}, \tag{1}$$

where $E(x,y)$ and $E'(x,y)$ are the field magnitudes of the modes at location (x,y) in the system before and after perturbation, respectively. $\bar{E}$ and $\bar{E}'$ represent the mean field values of the corresponding modes. The C_E value quantifies the similarity between the modes before and after the perturbation, and for the system shown in Fig. 2, it is found to be 0.92, 0.95, 0.99, and 0.99 for modes 1, 2, 3, and 4, respectively. The C_E values indicate that the perturbation leads to more changes in modes 1 and 2 as compared to modes 3 and 4. It is evident from Figs. 2(e)–2(h) that the perturbed scatterer is present in the region with high field value for modes 1 and 2 as compared to modes 3 and 4. Thus, a perturbation in the high field region of a mode leads to more changes in the lasing modes as compared to a perturbation in the low field region. It is also observed that the shape of the spatial field profiles of modes does not change drastically after the perturbation. However, minute changes are observed in the distribution of the field and its magnitude. Moreover, the perturbation also leads to changes in the spectral location of the lasing modes. The spectral shift ($\Delta\lambda$) in the modes is linearly related to C_E value as shown in Fig. 3. For modes exhibiting small changes in their spectral position, the C_E values are found to be ∼1, and as $\Delta\lambda$ increases, C_E decreases. Thus, with increasing spectral shift the changes in the field distribution of the corresponding modes become more prominent.

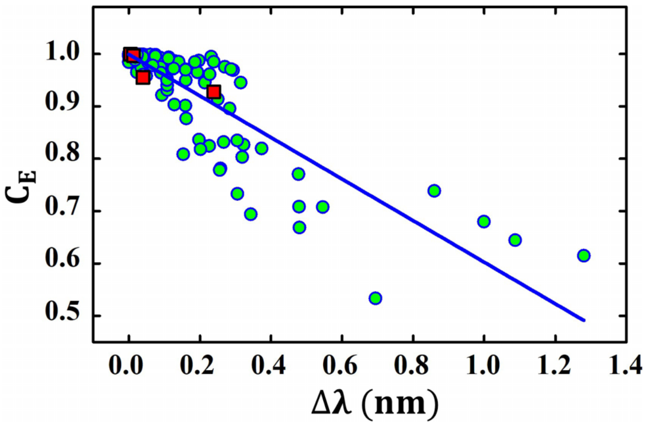

FIG. 3. Variation of C_E with the spectral shift ($\Delta\lambda$) in the lasing modes due to perturbation introduced in the system. The solid line represents the linear fit to the data points. The data points marked in red squares correspond to modes 1–4 in Fig. 2.

The sensitivity of lasing modes to nanoscale displacements has been utilized to monitor perturbations in the system. It is observed that the nanoscale alteration in the scatterer position leads to changes in the lasing modes and their spatial field distributions, and the amount of change varies for each mode. The effect of perturbation is prominent for the modes having a considerable field value around the perturbed particle. But, these changes in the individual modes do not provide any information about the position of the perturbed particle. Now, it is interesting to ask whether one can identify the particle that has been perturbed, given the modes before and after the perturbation are known. Here, we show that it is possible to locate the position of the scatterer that has been perturbed with the help of the computed modes by defining a tracking parameter TP as

$$\mathrm{TP}(x,y) = \prod_m \left| \frac{E_m(x,y)}{\max(E_m)} - \frac{E'_m(x,y)}{\max(E'_m)} \right|, \tag{2}$$

where $E_m(x,y)$ and $E'_m(x,y)$ are the field values of mode m before and after the perturbation at the (x,y) position in the system, respectively. $\max(E_m)$ and $\max(E'_m)$ represent the maximum values in the electric field distribution of the mode m before and after the perturbation, respectively. The tracking parameter is given by the product of change in the field distribution of the modes considered, due to perturbation. Here, the normalized field values have been considered, as we are interested in how the field at a point in the system changes with respect to its neighboring positions with perturbation.

In Fig. 4(a), TP shows the impact of perturbation on a single mode of the system. This contrasts with Fig. 2, which shows that modes are rather preserved after perturbation. Thus, for $N = 1$, TP quantifies the impact of perturbation on a single mode and implies that a single mode is indeed sensitive to any small change in the system, but it fails to

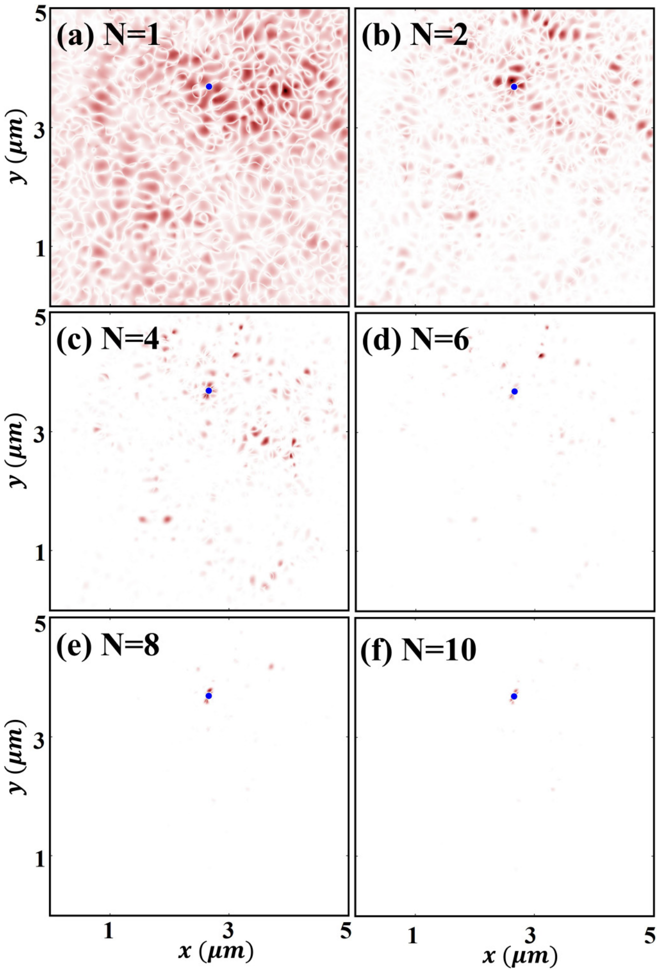

FIG. 4. The maps generated to locate the position of perturbed particle with the help of TP. The TP mapped regions when number of modes (a) $N = 1$, (b) $N = 2$, (c) $N = 4$, (d) $N = 6$, (e) $N = 8$, and (f) $N = 10$ are considered for the particle perturbed by 10 nm at location 1 (Fig. 1). The perturbed particle is marked in blue.

identify the location of perturbation. Further, when two modes are considered, a significant reduction in the region mapped by TP is observed as shown in Fig. 4(b). As the number of modes considered to evaluate TP is increased further, the TP mapped region reduces and concentrates around the perturbed particle as shown in Figs. 4(c)–4(f). Thus, when a cumulative effect of perturbation is considered for multiple modes of the system, TP provides a way to locate the perturbed particle. The accuracy of the localization of the perturbation increases with the number of modes considered to evaluate TP. Here, we were limited to ten modes, but by considering more modes (larger system, larger spectral range) the localization can be improved further.

Next, to understand the consistency of the proposed approach to locate perturbation, a single particle was displaced at different locations in the system along arbitrary directions by 10 nm. Figures 5(a)–5(d) show how the accuracy of the localization of the defect fluctuates from place to place in the system, when ten modes are considered to evaluate TP. It is observed that the perturbed particle lies within the mapped region for the perturbation at different locations in the system.

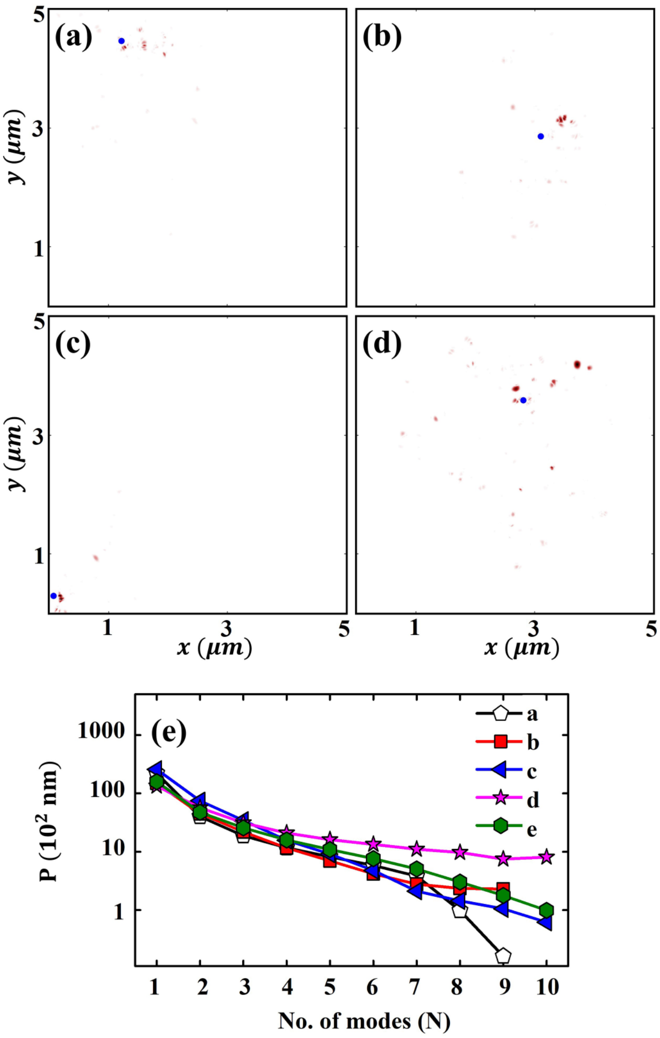

FIG. 5. (a–d) Maps generated with the help of TP to locate the position of a particle perturbed by 10 nm at different locations in the system. The perturbed particle is marked in blue. (e) The proximity parameter P as a function of number of modes (N) for systems in (a)–(d) and for the system in Fig. 4 [marked as (e)].

In order to quantify the accuracy to which the location of perturbation has been identified, a proximity parameter has been calculated as a function of number of modes considered. The proximity parameter P is defined as the root mean square of the distance of the perturbed particle from each point in the tracking parameter mapped region having a TP value of at least $\frac{1}{e}$ times the maximum TP value. The value of P is defined as follows:

$$P = \sqrt{\frac{1}{n}\sum_i d_i^2}, \qquad d_i = \sqrt{(x_p - x_i)^2 + (y_p - y_i)^2}. \tag{3}$$

Here, d_i is the distance of perturbed particle at (x_p, y_p) from the location (x_i, y_i) in the region mapped with TP. Figure 5(e) shows how the value of P changes when different numbers of modes are considered. The value of P for systems in Figs. 5(a)–5(d) are marked as (a)–(d) in Fig. 5(e). Plot (e) in Fig. 5(e) corresponds to the system perturbed at location 1 in Fig. 1, for which the variation of TP for different numbers of

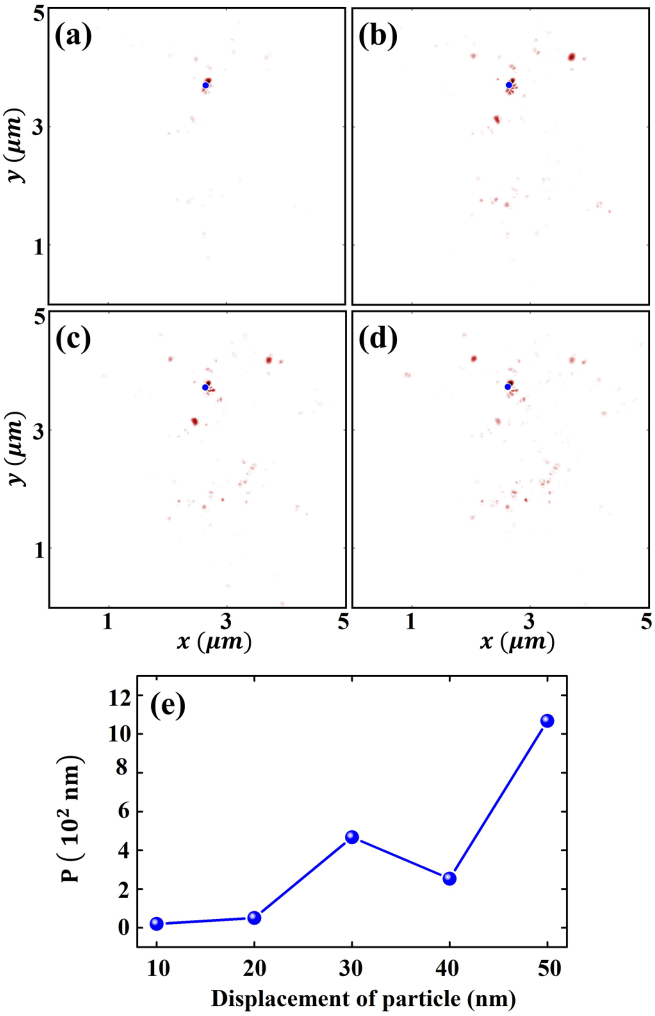

FIG. 6. Maps generated with the help of TP to locate the position of a particle perturbed by (a) 20, (b) 30, (c) 40, and (d) 50 nm at location 1 in the system. The perturbed particle is marked in blue. (e) The proximity parameter for different values of displacements in (a)–(d).

modes considered is shown in Fig. 4. In Fig. 5(e), it is observed that as the number of modes considered increases, the proximity parameter value decreases, i.e., the region mapped with TP gives a more accurate estimate of the location of perturbation.

To investigate the applicability of the proposed method for larger displacements, the particle perturbed at location 1 in Fig. 1 is subjected to displacements of 20–50 nm along an arbitrary direction. It is observed that, for larger displacements, the changes in the mode locations and their corresponding spatial field distributions become more prominent. The region mapped with the help of TP and the displaced particle (marked in blue) are shown in Figs. 6(a)–6(d) when a single particle is perturbed by (a) 20, (b) 30, (c) 40, and (d) 50 nm. It is observed that as the displacement increases, the mapped regions becomes wider. This result is supported by the proximity parameter values in Fig. 6(e). Effectively, the tracking parameter can be applicable to accurately identify single-step displacements of ~ 20 nm or smaller. Larger displacements can also be accurately mapped if they are carried out in multiple steps of ~ 20 nm.

IV. CONCLUSION

In summary, a numerical study on the detection and localization of nanoscale perturbation in a 2D strongly scattering active disordered system has been presented. The modes and the corresponding spatial field distributions have been calculated by solving Maxwell's equation combined with rate equations for a four-level atomic system. A tracking parameter has been proposed to identify the region of nanoscale perturbation. It is shown that the tracking parameter can map the regions of perturbation very well for single-nanoscale perturbations. The results presented in this paper demonstrate that nanoscale perturbations in a system can be tracked if the spatial field distribution of the modes before and after the perturbation is known. Thus, RLs have been proposed as a tool to track minute changes taking place in a disordered system. As of now, the tracking parameter can be evaluated with the help of tailored pump intensity profiles used for selective excitation of modes. It was demonstrated recently that localized modes of a one-dimensional random laser can be selected and mapped individually [40]. Our method can be easily tested in this system. It can prove to be useful in biomedical applications to track the minute growth of tumors in cells. Imaging methods such as x-ray, CT scan, etc., can be used to locate the region of diagnosis, and then detailed monitoring of tumors can be carried out with the proposed method. The formulated TP works well for strongly scattering systems, due to the localized nature of the lasing modes. In weakly scattering diffusive systems, the modes are extended all over the system, and any perturbation in the system leads to changes in a wide area around the perturbed particle. Hence, TP maps a wide region and the perturbed particle cannot be located accurately. The proposed TP is to be modified for weakly scattering diffusive systems. At present, the TP takes into account the change in the spatial field distribution of the modes, but the contribution of the spectral shifts in the lasing modes also need to be considered for the case of weakly scattering systems.

ACKNOWLEDGMENTS

The authors acknowledge Jonathan Andreasen, Georgia Tech Research Institute, and Anirban Sarkar, National Institute of Technology, Calicut, for fruitful discussions and help in computation. We acknowledge support from the Science and Engineering Research Board via sponsered Project No. CRG/2020/002650. The DST-FIST facility, Department of Physics, IIT Kharagpur, is acknowledged for computational support. We acknowledge the National Supercomputing Mission (NSM) for providing the computing resources of PARAM Shakti at IIT Kharagpur, which is implemented by C-DAC and supported by the Ministry of Electronics and Information Technology (MeitY), Department of Science and Technology (DST), Government of India. The Israel Science Foundation (Grants No. 1871/15, No. 2074/15, and No. 2630/20) and the United States-Israel Binational

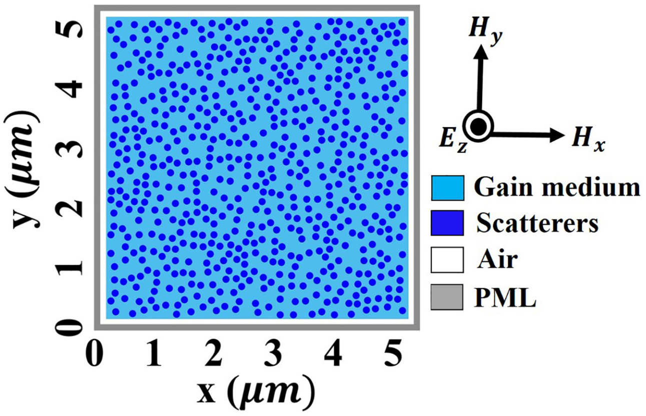

FIG. 7. The 2D disordered system considered for simulation.

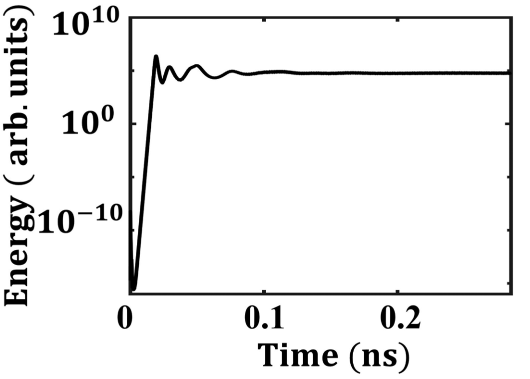

FIG. 8. Semilogarithmic representation of energy of RL system as a function of time, recorded during the growth of laser emission above the lasing threshold.

Science Foundation NSF/BSF (Grants No. 2015694 and No. 2021811) are acknowledged.

APPENDIX: FDTD COMPUTATION ALGORITHM AND NUMERICAL DETAILS

A 2D system of size $L^2 = 5 \times 5\ \mu\text{m}^2$ has been considered. The system consists of circular scatterers of radius $r = 60$ nm and refractive index $n_2 = 2.54$, randomly distributed in an active background medium of refractive index $n_1 = 1.53$ as shown in Fig. 7. The active medium is modeled as a four-level atomic system. The surface filling fraction of the scatterers is 28%. This system is similar to a random distribution of circular cylinders extending infinitely along the z direction. In order to look at the interplay of gain and disorder, the Maxwell's equations are coupled with the rate equations for the active system [41]. The perfectly matched layer (PML) boundary conditions have been used to simulate an open system. These are absorbing boundary conditions and prevent any spurious reflections at the boundary which otherwise would alter the lasing action in the system [42,43]. A 2D FDTD computation can be carried out using the transverse electric (TE) or transverse magnetic (TM) fields with respect to the z axis. For further computations, a TM field has been considered. Here, a TM field corresponds to the electric field normal to the plane of the modeled structure (E_Z) and magnetic field in the plane of the system (H_x, H_y) as shown in Fig. 7. The Maxwell's equations for a TM field are as follows:

$$\mu_0 \frac{\partial H_x}{\partial t} = -\frac{\partial E_z}{\partial y} \tag{A1}$$

$$\mu_0 \frac{\partial H_y}{\partial t} = \frac{\partial E_z}{\partial x} \tag{A2}$$

$$\varepsilon_i \varepsilon_0 \frac{\partial E_z}{\partial t} = \frac{\partial H_y}{\partial x} - \frac{\partial H_x}{\partial y}, \tag{A3}$$

where ε_0 and μ_0 are the electric permittivity and the magnetic permeability of the vacuum, respectively, and $\varepsilon_i = n_i^2$ ($i = 1, 2$), where n_i is the refractive index of the medium considered.

The active background medium is modeled as a four-level atomic system. This introduces a polarization term in the Maxwell's equations,

$$\mu_0 \frac{\partial H_x}{\partial t} = -\frac{\partial E_z}{\partial y} \tag{A4}$$

$$\mu_0 \frac{\partial H_y}{\partial t} = \frac{\partial E_z}{\partial x} \tag{A5}$$

$$\varepsilon_i \varepsilon_0 \frac{\partial E_z}{\partial t} + \frac{\partial \mathbf{P}}{\partial t} = \frac{\partial H_y}{\partial x} - \frac{\partial H_x}{\partial y}, \tag{A6}$$

where $\mathbf{P}$ is the polarization density.

The time evolution of populations N_i in the four-level atomic system is described by the following rate equations [44]:

$$\frac{dN_1}{dt} = \frac{N_2}{\tau_{21}} - W_p N_1 \tag{A7}$$

$$\frac{dN_2}{dt} = \frac{N_3}{\tau_{32}} - \frac{N_2}{\tau_{21}} - \frac{E_z}{\hbar\omega_l}\frac{d\mathbf{P}}{dt} \tag{A8}$$

$$\frac{dN_3}{dt} = \frac{N_4}{\tau_{43}} - \frac{N_3}{\tau_{32}} + \frac{E_z}{\hbar\omega_l}\frac{d\mathbf{P}}{dt} \tag{A9}$$

$$\frac{dN_4}{dt} = -\frac{N_4}{\tau_{43}} + W_p N_1, \tag{A10}$$

where W_p is the pump rate at which the electrons are excited from level 1 to level 4. The electrons in level 4 relax quickly to level 3 via a nonradiative process with a characteristic time τ_{43} and the population in level 3 builds up. Level 3 and level 2 are the upper and the lower lasing levels, respectively. The lasing transition occurs at the frequency $\omega_l = \frac{E_3 - E_2}{\hbar}$.The electrons in level 3 can decay to level 2 through spontaneous emission with the decay rate τ_{32} or through stimulated emission with the rate $\frac{E_z}{\hbar\omega_l}\frac{d\mathbf{P}}{dt}$. Then, the electrons in level 2 relax quickly to level 1 with a time constant τ_{21}. Here, E_z, $\mathbf{P}$, and N_i ($i = 1$–4) are the functions of r and t. The polarization is given as per the following equation [44]:

$$\frac{d^2\mathbf{P}}{dt^2} + \Delta\omega_l \frac{d\mathbf{P}}{dt} + \omega_l^2 \mathbf{P} = \kappa \Delta N E_z, \tag{A11}$$

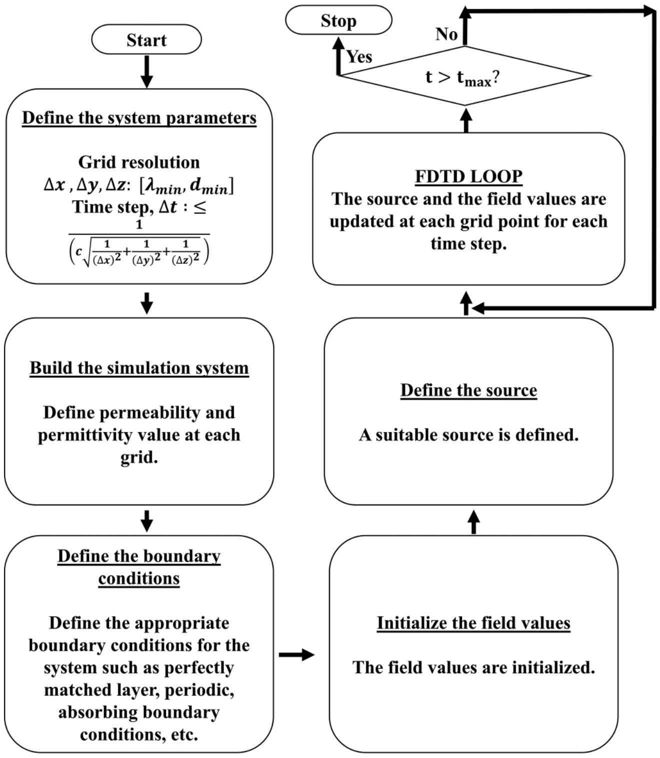

FIG. 9. Flowchart of the FDTD algorithm.

where $\Delta N = N_2 - N_3$ is the population density difference between the two lasing levels. The amplification takesplace when the population inversion ($\Delta N < 0$) is achieved. $\Delta\omega_l$ is the linewidth of the atomic transition, $\Delta\omega_l = \frac{1}{\tau_{32}} + \frac{2}{T_2}$, where T_2 is the collision time. It is usually much smaller than the lifetime τ_{32}. The constant κ is given by $\kappa = \frac{3c^3}{2\omega_l^2\tau_{32}}$ [44]. The parameters used for numerical simulations are as follows:

(1) Total atomic density, $N_T = 3.3 \times 10^{24}$ m^{-3}

(2) Frequency of the atomic transition, $\nu_l = \frac{\omega_l}{2\pi} = 4.85 \times 10^{14}$ Hz

(3) Lifetime of level 4, $\tau_{43} = 1 \times 10^{-13}$ s

(4) Lifetime of level 3, $\tau_{32} = 1 \times 10^{-10}$ s

(5) Lifetime of level 2, $\tau_{21} = 5 \times 10^{-12}$ s

(6) Collision time, $T_2 = 2 \times 10^{-14}$ s

The numerical parameters chosen are close to the dye molecules such as DCM. The values have been chosen a little bit shorter in order to reduce the computation time needed to achieve a stationary state. However, care has been taken to maintain a good separation of the time scales associated with the different relaxation processes. In general, the final equations which need to be solved are

$$\frac{\partial \mathbf{H}}{\partial t} = -c\nabla \times \mathbf{E} \tag{A12}$$

$$\varepsilon(r)\frac{\partial \mathbf{E}}{\partial t} = c\nabla \times \mathbf{H} - 4\pi\frac{\partial \mathbf{P}}{\partial t}. \tag{A13}$$

In order to solve Eqs. (A4)–(A6) by the FDTD method, they are discretized in space and time by Yee's algorithm [38,45]. The whole computation domain is divided into grids. The permittivity and permeability parameters are assigned at each grid point. The chosen grid size should be sufficient to resolve the smallest dimension of the system. Here, a grid size of 10 nm has been considered along the x and y directions ($\Delta x = \Delta y = 10$ nm). The time step has been chosen in accordance with Courant stability criterion to ensure the stability of the FDTD algorithm, $\Delta t = \frac{\Delta x}{c\sqrt{2}} = 2.37 \times 10^{-17}$ s, where c is the speed of light [38]. In order to simulate an open system, PML boundary conditions have been applied as stated earlier. The PML layer is chosen to be 10 cells thick ($10 \times \Delta x$) in order to minimize the reflection losses at the outer boundary of the PML [38]. In principle, the laser action initiates from noise; however, in the semiclassical description used here, the noise is not modeled and a seed is needed to start the laser action. So, the system is pumped uniformly with a Gaussian pulse of central wavelength 532 nm and pulse duration $\sim 10^{-15}$ s with a pump rate $W_p = 7.8 \times 10^8$ m^{-3}, well above the lasing threshold of the system. The Gaussian source is given as

$$A(t) = A_0 e^{-\frac{(t-t_0)^2}{2dt^2}} \sin[2\pi f_s(t - t_0)], \tag{A14}$$

where A_0 is the initial amplitude of the source, f_0 is the carrier frequency, and dt is the pulse half-width.

As the system is pumped above the lasing threshold, the energy in the system is observed to grow exponentially, and after some strong relaxation oscillations, it eventually reaches a steady state as shown in the Fig. 8.

So, the simulation needs to be run for a sufficient time for the system to become stable. The field is calculated at each grid point for each time step using the discretized update equations mentioned in Ref. [34]. After the system has reached the steady state, the emission spectrum of the system can be obtained by taking the Fourier transforms of the time records of the field. The spatial field distribution for each mode can be computed by Fourier transform of the field recorded at each grid point for the corresponding mode frequency. The flowchart for the FDTD algorithm is shown in Fig. 9.

---

[1] V. Letokhov, Sov. Phys. JETP **26**, 835 (1968).
[2] A. Tulek and Z. Vardeny, J. Opt. **12**, 024008 (2010).
[3] J. Lü, T. Fan, and G. Chen, Opt. Commun. **356**, 17 (2015).
[4] H. Cao, Y. G. Zhao, S. T. Ho, E. W. Seelig, Q. H. Wang, and R. P. H. Chang, Phys. Rev. Lett. **82**, 2278 (1999).
[5] Q. Song, S. Xiao, Z. Xu, J. Liu, X. Sun, V. Drachev, V. M. Shalaev, O. Akkus, and Y. L. Kim, Opt. Lett. **35**, 1425 (2010).
[6] N. M. Lawandy, R. Balachandran, A. Gomes, and E. Sauvain, Nature (London) **368**, 436 (1994).
[7] B. Shivakiran Bhaktha, N. Bachelard, X. Noblin, and P. Sebbah, Appl. Phys. Lett. **101**, 151101 (2012).
[8] S. Ferjani, V. Barna, A. De Luca, C. Versace, and G. Strangi, Opt. Lett. **33**, 557 (2008).
[9] H. Cao, Waves Random Media **13**, R1 (2003).
[10] P. Sebbah and C. Vanneste, Phys. Rev. B **66**, 144202 (2002).

[11] X. Jiang and C. M. Soukoulis, Phys. Rev. E **65**, 025601(R) (2002).

[12] J. Andreasen, A. Asatryan, L. Botten, M. Byrne, H. Cao, L. Ge, L. Labonté, P. Sebbah, A. Stone, H. Türeci *et al.*, Adv. Opt. Photon. **3**, 88 (2011).

[13] C. Vanneste, P. Sebbah, and H. Cao, Phys. Rev. Lett. **98**, 143902 (2007).

[14] C. Gouedard, D. Husson, C. Sauteret, F. Auzel, and A. Migus, JOSA B **10**, 2358 (1993).

[15] M. Noginov, S. Egarievwe, N. Noginova, H. Caulfield, and J. Wang, Opt. Mater. (Amsterdam) **12**, 127 (1999).

[16] B. Redding, M. A. Choma, and H. Cao, Opt. Lett. **36**, 3404 (2011).

[17] B. Redding, M. A. Choma, and H. Cao, Nat. Photonics **6**, 355 (2012).

[18] S.-W. Chang, W.-C. Liao, Y.-M. Liao, H.-I. Lin, H.-Y. Lin, W.-J. Lin, S.-Y. Lin, P. Perumal, G. Haider, C.-T. Tai *et al.*, Sci. Rep. **8**, 2720 (2018).

[19] S. P. Mallick and Z. Sung, Ann. Phys. **532**, 2000323 (2020).

[20] N. Bachelard, J. Andreasen, S. Gigan, and P. Sebbah, Phys. Rev. Lett. **109**, 033903 (2012).

[21] T. Hisch, M. Liertzer, D. Pogany, F. Mintert, and S. Rotter, Phys. Rev. Lett. **111**, 023902 (2013).

[22] S. F. Liew, B. Redding, L. Ge, G. S. Solomon, and H. Cao, Appl. Phys. Lett. **104**, 231108 (2014).

[23] S. F. Liew, L. Ge, B. Redding, G. S. Solomon, and H. Cao, Phys. Rev. A **91**, 043828 (2015).

[24] L. Ge, Opt. Express **23**, 30049 (2015).

[25] N. Bachelard, S. Gigan, X. Noblin, and P. Sebbah, Nat. Phys. **10**, 426 (2014).

[26] B. Kumar, R. Homri, Priyanka, S. K. Maurya, M. Lebental, and P. Sebbah, Optica **8**, 1033 (2021).

[27] S. Ho Choi and Y. L. Kim, Appl. Phys. Lett. **100**, 041101 (2012).

[28] R. C. Polson and Z. V. Vardeny, Appl. Phys. Lett. **85**, 1289 (2004).

[29] M. Siddique, L. Yang, Q. Wang, and R. Alfano, Opt. Commun. **117**, 475 (1995).

[30] Q. Song, Z. Xu, S. H. Choi, X. Sun, S. Xiao, O. Akkus, and Y. L. Kim, Biomed. Opt. Express **1**, 1401 (2010).

[31] R. Polson and Z. Vardeny, J. Opt. **12**, 024010 (2010).

[32] Y. Wang, Z. Duan, Z. Qiu, P. Zhang, J. Wu, D. Zhang, and T. Xiang, Sci. Rep. **7**, 8385 (2017).

[33] M. Hohmann, D. Dörner, F. Mehari, C. Chen, M. Späth, S. Müller, H. Albrecht, F. Klämpfl, and M. Schmidt, Biomed. Opt. Express **10**, 807 (2019).

[34] A. Taflove, S. C. Hagness, and M. Piket-May, Electr. Eng. Handbook **3**, 629 (2005).

[35] A. Sarkar, N. S. Ojha, and B. S. Bhaktha, Appl. Phys. Lett. **110**, 251104 (2017).

[36] P. S. Choubey, S. Ghosh, S. K. Varshney, and S. B. BN, J. Phys. D **53**, 245104 (2020).

[37] P. S. Choubey, A. Sarkar, S. K. Varshney, and S. B. BN, JOSA B **37**, 2505 (2020).

[38] K. Yee, IEEE Trans. Antennas Propag. **14**, 302 (1966).

[39] H. C. Hulst and H. C. van de Hulst, *Light Scattering by Small Particles* (Courier Corporation, North Chelmsford, 1981).

[40] B. Kumar and P. Sebbah, in *CLEO: QELS_Fundamental Science* (Optica Publishing Group, Washington DC, 2022), pp. JW3B–66.

[41] X. Jiang and C. M. Soukoulis, Phys. Rev. Lett. **85**, 70 (2000).

[42] J.-P. Berenger, J. Comput. Phys. **114**, 185 (1994).

[43] H. Cao, Y. Zhao, X. Liu, E. Seelig, and R. Chang, Appl. Phys. Lett. **75**, 1213 (1999).

[44] A. E. Siegman, *Lasers* (University Science Books, Sausalito, 1986).

[45] A. Taflove, IEEE Trans. Electromagn. Compatibility **EMC-22**, 191 (1980).